Interpretation of magnetic data using tilt-angle derivatives

Article *in* Geophysics · January 2008

DOI: 10.1190/1.2799992

5 authors, including:

Ahmed S. Salem

77 PUBLICATIONS **1,615** CITATIONS

SEE PROFILE

Simon Williams

Northwest University

137 PUBLICATIONS **3,001** CITATIONS

SEE PROFILE

Richard Stuart Smith

Laurentian University

145 PUBLICATIONS **2,176** CITATIONS

SEE PROFILE

Dhananjay Ravat

University of Kentucky

131 PUBLICATIONS **2,599** CITATIONS

SEE PROFILE

GEOPHYSICS, VOL. 73, NO. 1 (JANUARY-FEBRUARY 2008); P. L1–L10, 7 FIGS.
10.1190/1.2799992

Interpretation of magnetic data using tilt-angle derivatives

Ahmed Salem[1], Simon Williams[1], Derek Fairhead[1,2], Richard Smith[3], and Dhananjay Ravat[4]

ABSTRACT

We have developed a new method for interpretation of gridded magnetic data which, based on derivatives of the tilt angle, provides a simple linear equation, similar to the 3D Euler equation. Our method estimates both the horizontal location and the depth of magnetic bodies, but without specifying prior information about the nature of the sources (structural index). Using source-position estimates, the nature of the source can then be inferred. Theoretical simulations over simple and complex magnetic sources that give rise to noise-corrupted and noise-free data, illustrate the ability of the method to provide source locations and index values characterizing the nature of the source bodies. Our method uses second derivatives of the magnetic anomaly, which are sensitive to noise (high-wavenumber spectral content) in the data. Thus, an upward continuation of the anomaly may lead to reduce the noise effect. We demonstrate the practical utility of the method using a field example from Namibia, where the results of the proposed method show broad correlation with previous results using interactive forward modeling.

INTRODUCTION

One important goal in the interpretation of magnetic data is to determine the type and the location of the magnetic source. This has recently become particularly important because of the large volumes of magnetic data that are being collected for environmental and geological applications. To this end, a variety of semiautomatic methods, based on the use of derivatives of the magnetic field, have been developed to determine magnetic source parameters such as locations of boundaries and depths (e.g., see references in Blakely, 1995; Nabighian et al., 2005). As faster computers and commercial software have become widely available, these techniques are being used more extensively.

Utilizing first-order derivatives of the magnetic field, Euler deconvolution was first presented by Thompson (1982) for profile data and by Reid et al. (1990) for gridded data. The method has come into wide use as an aid for interpreting magnetic data (FitzGerald et al., 2004). The main advantage of the Euler method is that it can provide automatic estimates of the source location of the causative magnetic anomalies. However, it requires an assumption about the type of body that is the nature source. In practice, this is achieved by specifying a structural index η to define the source type in generalized situations, setting a good strategy for discriminating, and selecting meaningful solutions. Recent extensions to the Euler method allow η to be estimated from the data, with the calculation of Hilbert transforms of the derivatives (Nabighian and Hansen, 2001).

Thurston and Smith (1997) presented the SPI method, which requires second-order derivatives of the field. The SPI method uses a term known as the local wavenumber to provide a rapid estimate of the depth of buried magnetic bodies. The local wavenumber was defined as the spatial derivative of the local phase. The SPI method works on gridded data, but assumed a contact model ($\eta = 0$). Later extensions to the method (Smith et al., 1998; Thurston et al., 2002) enabled calculation of η, but these required third-order derivatives. The calculation of third-order derivatives from gridded data is problematic so the use of profile data was advocated by Smith et al. (2005) and Smith and Salem (2005).

Very recently, several new approaches have been developed that deal with depth determination and structural index estimation simultaneously. One method (Fedi, 2007) calculates the field at many altitudes and scales the field by a power law of the altitude. The depth and index can be obtained by finding extreme points. Another method (Stavrev and Reid, 2007) assumes (like the Euler method) homogeneous potential fields, but applies a similarity transform.

Salem et al. (2005) presented the enhanced local wavenumber method (ELW) for interpreting profile magnetic data. Based on the 2D Euler equation (Thompson, 1982), they showed that deconvolution of the derivatives of the local phase can provide automatic esti-

Manuscript received by the Editor 11 April 2007; revised manuscript received 8 August 2007; published online 16 November 2007.
[1]GETECH, Leeds, U.K. E-mail: ahmedsalem30@yahoo.com; sw@getech.com.
[2]University of Leeds, School of Earth & Environment, U.K. E-mail: jdf@getech.com.
[3]Fugro Airborne Surveys, Ontario, Canada. E-mail: rsmith@fugroairborne.com.
[4]University of Kentucky, Earth & Environmental Sciences, Lexington, Kentucky. E-mail: dhananjay.ravat@uky.edu.

mates of the source location regardless of the nature of the sources. The tilt angle is similar to the local phase, used in the ELW method for profile magnetic data. The local phase uses the sign of the horizontal gradient, whereas the tilt angle uses the absolute value.

The purpose of this paper is to show that the derivatives of the tilt angle can provide an automatic estimate of the source location from gridded magnetic data. Our objectives are to derive information about depth of the magnetic sources and the structural index (η). We use second-order derivatives of the field. Thus our method has potential advantages over methods requiring third-order derivatives.

METHOD

The tilt angle (Miller and Singh, 1994; Verduzco et al., 2004) is defined as

$$\theta = \tan^{-1}\left[\frac{\dfrac{\partial M}{\partial z}}{\dfrac{\partial M}{\partial h}}\right], \tag{1}$$

where

$$\frac{\partial M}{\partial h} = \sqrt{\left(\frac{\partial M}{\partial x}\right)^2 + \left(\frac{\partial M}{\partial y}\right)^2}, \tag{2}$$

and $\partial M/\partial x$, $\partial M/\partial y$, and $\partial M/\partial z$ are the derivatives of the magnetic field M in the x, y and z directions. We define the rate of change of the tilt angle θ with respect to the x, y, and z directions as the wavenumbers:

$$k_x = \frac{\partial \theta}{\partial x} = \frac{1}{A^2}\left(\frac{\partial M}{\partial h}\frac{\partial^2 M}{\partial x \partial z} - \frac{\partial M}{\partial z}\left(\frac{\partial M}{\partial h}\right)^{-1} \times\left(\frac{\partial M}{\partial x}\frac{\partial^2 M}{\partial x^2} + \frac{\partial M}{\partial y}\frac{\partial^2 M}{\partial y \partial x}\right)\right), \tag{3}$$

$$k_y = \frac{\partial \theta}{\partial y} = \frac{1}{A^2}\left(\frac{\partial M}{\partial h}\frac{\partial^2 M}{\partial y \partial z} - \frac{\partial M}{\partial z}\left(\frac{\partial M}{\partial h}\right)^{-1} \times\left(\frac{\partial M}{\partial x}\frac{\partial^2 M}{\partial x \partial y} + \frac{\partial M}{\partial y}\frac{\partial^2 M}{\partial y^2}\right)\right), \tag{4}$$

and

$$k_z = \frac{\partial \theta}{\partial z} = \frac{1}{A^2}\left(\frac{\partial M}{\partial h}\frac{\partial^2 M}{\partial z^2} - \frac{\partial M}{\partial z}\left(\frac{\partial M}{\partial h}\right)^{-1} \times\left(\frac{\partial M}{\partial x}\frac{\partial^2 M}{\partial x \partial z} + \frac{\partial M}{\partial y}\frac{\partial^2 M}{\partial y \partial z}\right)\right), \tag{5}$$

where

$$A = \sqrt{\left(\frac{\partial M}{\partial x}\right)^2 + \left(\frac{\partial M}{\partial y}\right)^2 + \left(\frac{\partial M}{\partial z}\right)^2}$$

is the total gradient of the magnetic field.

The tilt angle has many interesting properties (Cooper and Cowan, 2006). For example, due to the nature of the arctan trigonometric function, all tilt values are restricted to values between $-\pi/2$ and $\pi/2$ regardless of the amplitude of the vertical derivative or the absolute value of the total horizontal gradient. This fact makes calculating the tilt angle similar to an automatic-gain-control filter: both operations tend to equalize the amplitude output of the magnetic anomalies across a grid or a profile (Verduzco et al., 2004). Our method utilizes the derivatives of the tilt angle to provide a direct estimate of the source location using the definition of the 3D Euler equation similar to Salem et al. (2005) for profile data. The 3D form of Euler's equation can be defined (Thompson, 1982; Reid et al., 1990) as

$$(x - x_o)\frac{\partial M}{\partial x} + (y - y_o)\frac{\partial M}{\partial y} + (z - z_o)\frac{\partial M}{\partial z} = \eta(B - M), \tag{6}$$

where x, y and z are the observation coordinates, x_o, y_o, and z_o are the source coordinates, B is base level and η is a value that describes the anomaly attenuation rate commonly known as the structural index. Taking the derivatives of the 3D Euler equation in the x, y, and z directions, we obtain

$$(x - x_o)\frac{\partial^2 M}{\partial x^2} + (y - y_o)\frac{\partial^2 M}{\partial y \partial x} + (z - z_o)\frac{\partial^2 M}{\partial z \partial x} = -(\eta + 1)\frac{\partial M}{\partial x}, \tag{7}$$

$$(x - x_o)\frac{\partial^2 M}{\partial x \partial y} + (y - y_o)\frac{\partial^2 M}{\partial y^2} + (z - z_o)\frac{\partial^2 M}{\partial z \partial y} = -(\eta + 1)\frac{\partial M}{\partial y}, \tag{8}$$

and

$$(x - x_o)\frac{\partial^2 M}{\partial x \partial z} + (y - y_o)\frac{\partial^2 M}{\partial y \partial z} + (z - z_o)\frac{\partial^2 M}{\partial z^2} = -(\eta + 1)\frac{\partial M}{\partial z}. \tag{9}$$

Multiplying equations 7 and 9 by

$$\left(\frac{1}{A^2}\frac{\partial M}{\partial z}\frac{\partial M}{\partial x}\right)$$

and

$$\left(\frac{1}{A^2}\left(\frac{\partial M}{\partial x}\right)^2\right),$$

respectively, and subtracting the first from the second, we obtain

$$\frac{(x - x_0)}{A^2}\left(\frac{\partial^2 M}{\partial x \partial z}\left(\frac{\partial M}{\partial x}\right)^2 - \frac{\partial^2 M}{\partial x^2}\frac{\partial M}{\partial x}\frac{\partial M}{\partial z}\right) + \frac{(y - y_0)}{A^2}\left(\frac{\partial^2 M}{\partial y \partial z}\left(\frac{\partial M}{\partial x}\right)^2 - \frac{\partial^2 M}{\partial y \partial x}\frac{\partial M}{\partial x}\frac{\partial M}{\partial z}\right) + \frac{(z - z_0)}{A^2}\left(\frac{\partial^2 M}{\partial z^2}\left(\frac{\partial M}{\partial x}\right)^2 - \frac{\partial^2 M}{\partial x \partial z}\frac{\partial M}{\partial x}\frac{\partial M}{\partial z}\right) = 0. \tag{10}$$

Multiplying equations 8 and 9 by

$$\left(\frac{1}{A^2}\frac{\partial M}{\partial z}\frac{\partial M}{\partial y}\right) \quad \text{and} \quad \left(\frac{1}{A^2}\left(\frac{\partial M}{\partial y}\right)^2\right),$$

respectively, followed by their subtraction, we obtain

$$\begin{aligned}\frac{(x-x_0)}{A^2}&\left(\frac{\partial^2 M}{\partial x\partial z}\left(\frac{\partial M}{\partial y}\right)^2-\frac{\partial^2 M}{\partial x\partial y}\frac{\partial M}{\partial y}\frac{\partial M}{\partial z}\right)\\ &+\frac{(y-y_0)}{A^2}\left(\frac{\partial^2 M}{\partial y\partial z}\left(\frac{\partial M}{\partial y}\right)^2-\frac{\partial^2 M}{\partial y^2}\frac{\partial M}{\partial y}\frac{\partial M}{\partial z}\right)\\ &+\frac{(z-z_0)}{A^2}\left(\frac{\partial^2 M}{\partial z^2}\left(\frac{\partial M}{\partial y}\right)^2-\frac{\partial^2 M}{\partial y\partial z}\frac{\partial M}{\partial y}\frac{\partial M}{\partial z}\right)=0.\end{aligned} \tag{11}$$

Adding 10 and 11 we obtain

$$\begin{aligned}\frac{(x-x_0)}{A^2}&\left(\left(\frac{\partial M}{\partial h}\right)^2\frac{\partial^2 M}{\partial x\partial z}-\frac{\partial M}{\partial z}\left(\frac{\partial M}{\partial x}\frac{\partial^2 M}{\partial x^2}+\frac{\partial M}{\partial y}\frac{\partial^2 M}{\partial x\partial y}\right)\right)\\ &+\frac{(y-y_0)}{A^2}\left(\left(\frac{\partial M}{\partial h}\right)^2\frac{\partial^2 M}{\partial y\partial z}-\frac{\partial M}{\partial z}\left(\frac{\partial M}{\partial x}\frac{\partial^2 M}{\partial x\partial y}\right.\right.\\ &\left.\left.+\frac{\partial M}{\partial y}\frac{\partial^2 M}{\partial y^2}\right)\right)+\frac{(z-z_0)}{A^2}\left(\left(\frac{\partial M}{\partial h}\right)^2\frac{\partial^2 M}{\partial z^2}\right.\\ &\left.-\frac{\partial M}{\partial z}\left(\frac{\partial M}{\partial x}\frac{\partial^2 M}{\partial x\partial z}+\frac{\partial M}{\partial y}\frac{\partial^2 M}{\partial z\partial y}\right)\right)=0.\end{aligned} \tag{12}$$

Dividing 12 by $\partial M/\partial h$ and substituting with the definitions of the tilt angle derivatives (equations 3–5), we obtain

$$k_x x_0 + k_y y_0 + k_z z_0 = k_x x + k_y y + k_z z. \tag{13}$$

The linear equation 13 is similar to the conventional 3D Euler equation, with the advantage that it does not require any prior information about the source geometry.

Various methods have been proposed for application of the Euler deconvolution method. A standard approach uses a progressively moving window (selected observations) and the solutions that are displayed are those that satisfy certain selection criteria. In each window, there are n data points having a known location (x,y,z) and tilt angle derivatives or wavenumbers (k_x,k_y,k_z). Hence, for each window, we have a matrix equation

$$\mathbf{Gm} = \mathbf{d}, \tag{14}$$

where $\mathbf{d}$ is an $n \times 1$ vector whose ith element is given by

$$k_{xi}x_i + k_{yi}y_i + k_{zi}z_i, \tag{15}$$

$\mathbf{G}$ is an $n \times 3$ matrix of tilt angle derivatives whose ith row has elements: $g_{i1} = k_{xi}$, $g_{i2} = k_{yi}$, and $g_{i3} = k_{zi}$, $i = 1,\ldots,n$, and a three-dimensional vector $\mathbf{m} \equiv [x_0\ y_0\ z_0]^T$ contains the unknown source location parameters.

Equation 14 is an overdetermined system and can be solved in a least-squares sense using standard techniques of linear inversion. Here, we suggest a simple strategy to automate the method and reject poorer solutions. In this strategy, we first calculate the total horizontal derivative term k_h of the tilt angle as

$$k_h = \sqrt{k_x^2 + k_y^2}. \tag{16}$$

The total horizontal derivative of the tilt angle is sharper than the total derivatives of the field (A) and generates better defined maxima centered over the 2D body edges (Verduzco et al., 2004). The peak locations of the grid of k_h are found using a method for detecting the peaks of a grid similar to that of Blakely and Simpson (1986). Our method uses the same Euler deconvolution's strategy of applying a moving data window to the magnetic anomaly. In contrast with the Euler deconvolution method, in our approach the moving data window spans only the x-, y-, and z-coordinates of the data points falling within a specified distance of the k_h peak locations to estimate the source location parameters (x_0,y_0,z_0). Once the source location (x_0, y_0, and z_0) has been obtained, a value for the structural index is estimated using one of equations 7, 8 or 9. The choice of data window size is a function of the data quality and the degree of interference of anomalies from nearby sources. For isolated anomalies, a larger data window can be used to overcome the effect of noise. For multiple neighboring sources, a smaller-size data window is appropriate to reduce interference effects. The solution is accepted based on the following criteria:

1) an accepted range based on the structural index (e.g., 0 to 2 for 2D sources)
2) an accepted range for the depth (e.g., source depths that the interpreter may accept as a possible solutions)
3) an acceptable estimates of horizontal source coordinates that should be close to the location of the detected k_h peak
4) an acceptable threshold of the estimates of the standard deviation from the least-squares solutions depending on the quality of the data (e.g. Thompson, 1982)

Other criteria are possible and are being investigated.

RESULTS AND DISCUSSION

In this section, we apply our method to interpreting noise-free and noise-corrupted magnetic data produced by simple and complex geologic settings. The first theoretical example (Figure 1a) consists of three sources — a vertical-sided prism (labeled A) at a depth of 3 km with a magnetization of 0.4 A/m, a vertical thin dike (labeled B) at a depth of 5 km with a magnetization of 5 A/m, and a second prism (labeled C) at a depth of 7 km with a magnetization 0.6 A/m. In this test, the magnetization is assumed induced by a field with an inclination of 90°. Figure 1b shows the tilt angle, while Figure 1c and d displays its total horizontal and vertical gradients, respectively. Following the strategy outlined above, we estimated of source locations and structural indices using a window size of 11×11 grid points. Solutions are computed for windows whose center points are within 2 km of peaks in the grid of k_h, and solutions are rejected if the estimated structural index is outside the acceptable range for 2D sources (from 0 to 2). Noise and errors may shift the indices from the ideal range. Therefore, the acceptance range may be slightly expanded (for example, from -0.2 to 2.2). Figure 1e and f displays the plan view of the estimates of the source locations and structural indices, respectively. The average depths are 3.02 ± 0.07 for prismatic source A, 5.28 ± 0.04 for thin dike B, and 6.91 ± 0.51 for prismatic source C. The results demonstrate the validity of the proposed strategy to accept an estimated solution as a possible solution for noise-free data. Our method provides accurate estimates of source depth and structural index for both the prism edges (0.04 ± 0.05 for model

A and 0.06 ± 0.05 for model C) and the thin dike (1.06 ± 0.02 for model B). Some inaccurate solutions are produced at the corners of the prisms, where the two edges act as interfering sources. It is worth noting that while many existing methods would produce accurate estimates of source depth for magnetic contacts and dikes, a number of these methods require that the source geometry is already known.

Because our method relies on second order derivatives of the observed field, we studied the effect that noise in the data has on the results. For this example, we used a vertical-sided prism centered at $x = 250$ km, $y = 250$ km, with its top at a depth of 5 km and effectively infinite depth extent. The prism has a magnetization of 0.1 A/m, and the inducing field has an inclination of 60° and a declination of 0°. The total field anomaly is calculated on a regular grid with a spacing of 1 km. The anomaly was corrupted with Gaussian noise with zero mean and a range of standard deviations, from 0.2 to 2 nT (note that the standard deviation of the original magnetic grid is 47.1 nT). For each noise-corrupted data set, the same strategy was used for the application of the derivatives of the tilt angle.

Solutions were calculated using a window size of 11×11 grid points for windows whose center points are located within 3 km of peaks in the grid k_h, and solutions are rejected if the estimated structural index is outside the acceptable range for 2D sources (-0.2 to 2.2). Even for relatively low levels of noise (e.g., standard deviation 0.2 nT), no solutions are found along the prism edges. In common with similar methods relying on high order derivatives for profile data (e.g., Salem and Ravat, 2003), we found that upward continuation of the noise-corrupted data stabilizes the results.

Figure 2a shows the total field anomaly data that has been corrupted with noise having a standard deviation of 2 nT and upward continued to 4 km. Figure 2b–d show the tilt angle, total horizontal gradient of the tilt angle, and vertical gradient of the tilt angle derived from the calculated total field anomaly data (Figure 2a). The noise produces many additional peaks in the grid of k_h even after upward continuation (Figure 2c). However, only windows located over the prism edges yield estimates of source location with structural indices within the acceptable range (-0.2 to 2.2). The accepted source coordinates are shown in plan view in Figure 2e, with the corresponding structural index estimates shown in Figure 2f. Figure 2g and h shows the perspective views of the estimated source depths and structural indices, illustrating the scattering of the solutions estimated at different data window positions. All depth values shown in these and subsequent plots have been adjusted for the appropriate upward continuation distance.

Figure 3 shows the effect of noise with different standard deviations on the estimates of source depth and structural index for two different continuation distances, 2 km and 4 km. The plotted points represent the mean percentage error in estimated depths (Figure 3a), standard deviation in depth (Figure 3b), the mean structural index (Figure 3c), and standard deviation in structural index (Figure 3d), for all estimates derived around the prism edges. The total number of accepted solutions varies for different noise levels and is always greater than 4000. In our tests, for relatively small amounts of noise, the depth estimates using the 2 km upward continuation distance are closer to the depth of the source, and have a smaller standard devia-

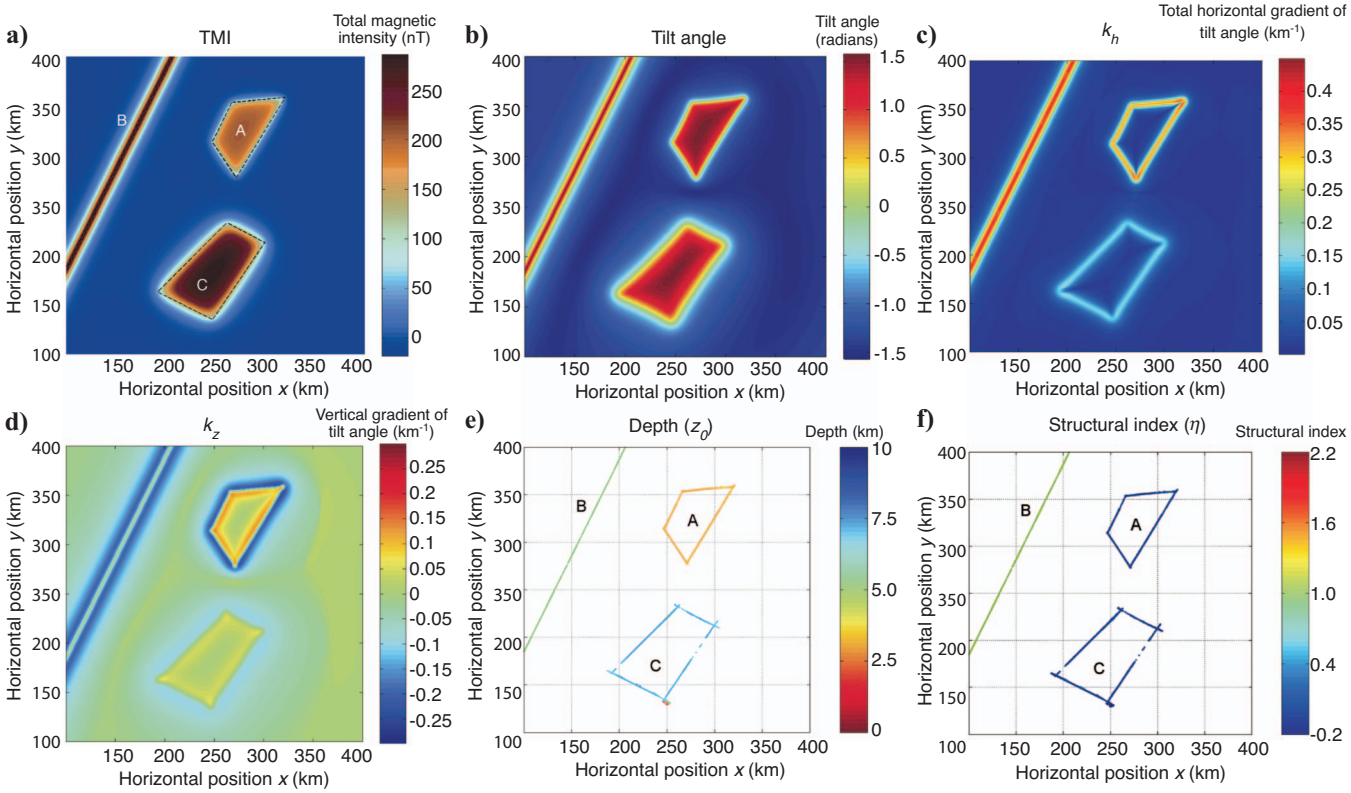

Figure 1. (a) Noise-free total magnetic intensity, obtained from the proposed method, at the pole for the synthetic model consisting of three simple sources (dashed lines); (b) tilt angle; (c) total horizontal derivative; (d) vertical derivative of tilt angle; (e) estimates of the source location; and (f) structural index.

tion. As the standard deviation of the noise increases, a greater continuation distance produced more accurate and less scattered estimates of depth and structural index.

The Bishop model

The Bishop 3D basement model has been used by various authors to test methods of estimating source depths from magnetic data (Williams et al. 2002, 2005; Fairhead et al., 2004; and Reid et al., 2005) and has been the subject of a workshop at the 2006 SEG annual meeting. The aim of the Bishop model is to provide a data set that shares the complexity of real magnetic data sets, but where our depth estimates can still be compared to the correct depths. The magnetic data are constructed from two input data sets. A topography grid defines the bounding surface between the sedimentary section (assumed to be nonmagnetic) and the magnetic basement. A magnetization grid divides the basement into terranes and intrusions, all with vertical contacts truncated at the top of the magnetic basement surface.

The topography grid is derived from a digital elevation model (DEM) for a 10.5 by 10.5 km area of the Volcanic Tablelands, north of Bishop, California. The DEM was scaled up to produce a 3D test model with dimensions 315 by 315 km on a 500-m grid, representative of a basin-scale magnetic basement surface (Figure 4a). The topographic surface datum was then shifted such that the highest point has a depth of a few hundred meters below datum (zero) and the deepest point lies just above 10 km depth. This topographic surface has been taken as the top of the magnetic basement with a magneti-

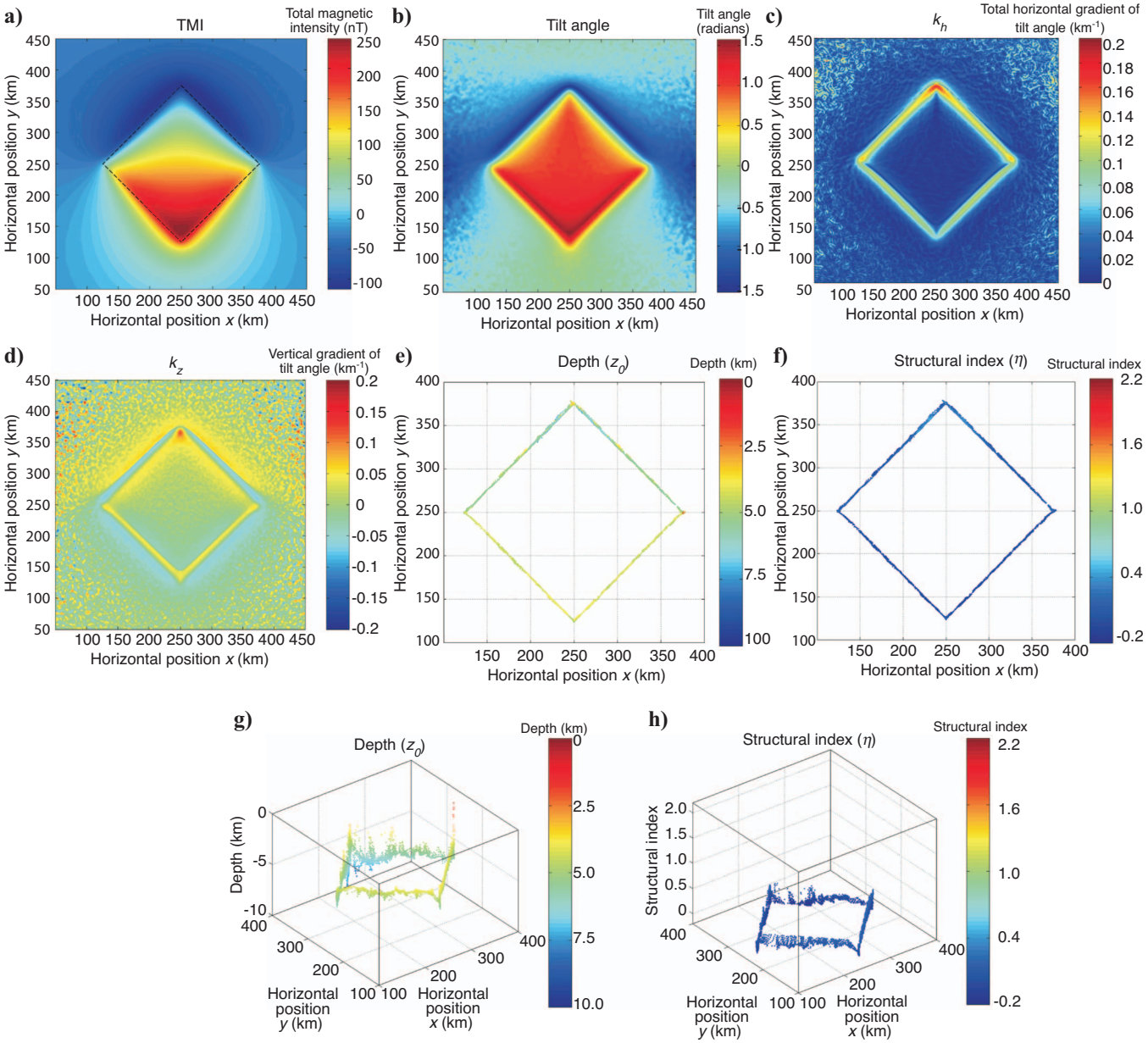

Figure 2. (a) Total magnetic intensity for the synthetic model containing a single prism source, corrupted by noise with 2 nT standard deviation and upward continued by 4 km; (b) tilt angle; (c) total horizontal derivative of tilt angle; (d) vertical derivative of tilt angle; (e) plan view of source location estimates; (f) structural index estimates; (g) 3D view of source location estimates; and (h) structural index estimates.

zation intensity defined by an additional grid (Figure 4b). The basement is assumed to extend down to 20 km depth and be overlain by nonmagnetic sediments.

Figure 4c shows the magnetic response for a basement susceptibility varying from 1.26×10^{-2} to 1.0×10^{-1} SI units and an ambient geomagnetic field with strength 50000 nT, inclination 90°, and declination 0°. The data are not corrupted by random noise, and have not been filtered. Figure 4d shows the tilt angle, while Figure 4e and f displays its total horizontal and vertical gradients respectively. The edges of features in the model such as strong magnetization contrasts correspond to zero-crossings in the grid of k_z (Figure 4f), though there are many additional zero-crossings that do not have an obvious correlation to features in the model basement. Peaks in the grid of k_h (Figure 4e) show a strong spatial correlation with the model basement structures — furthermore, the peak amplitudes are generally highest in the north-west part of the data where the model basement is shallowest, and have lower amplitudes in areas where the model basement depth is deep.

Figure 4g and h shows the estimates of the source location and structural index based on Euler deconvolution of the tilt angle. These results are derived using a window of 15×15 grid points (7 $\times$ 7 km). Solutions are calculated for windows with center points located within 1 km of peaks in the grid of k_h. We accept solutions according to the following criteria: if the x- and y-coordinate estimates of the sources locations lie within 2.5 km of peaks in the grid of k_h, if the estimated depth lies between 0 km and 15 km, and if the estimated structural index is between -0.2 and 2.2. We also use the standard deviation of the depth estimated from the least-squares solution. We reject solutions if the standard deviation of the estimated depth is greater than 12% of the estimated depth.

The overall pattern of estimated depths (Figure 4g) correlates reasonably well with the model basement depth. The estimates of the structural index (Figure 4h) are consistently in the range 0–0.5 over the two linear magnetization contrast sources in the basement, but show considerable scatter for other sources. For any individual source, the structural index values show a considerable amount of scatter. For nonhomogeneous sources, we would expect the structural index to vary with the position of the data window relative to the source (Ravat, 1996), so it is not surprising that window locations at different distances and different relative locations from a source give different structural index estimates.

The vertical scatter in the depth estimates is difficult to determine from Figure 4g alone, so we illustrate the degree of correlation between the depth estimates and true basement relief further with two cross sections. Figure 5a shows a northwest-southeast cross section through the Bishop model (profile A), perpendicular to the two linear terrane boundaries, whereas Figure 5b shows an east-west cross section (profile B), perpendicular to the dominant trend of topographic features in the model basement. For each cross section, the points plotted are all source location estimates within a band extending 4 km either side of the profile, projected onto the profile perpendicular to the profile direction.

We use these cross sections to compare the results of our method with those derived from 3D Euler deconvolution (Reid et al., 1990). The strategy for deriving these solutions is, where possible, consistent with that used for derivatives of the tilt angle method. The window size is 15×15 points, and solutions are derived only for windows with center points located within 1 km of peaks in the grid of k_h. To generate 3D Euler solutions we must assume a structural index, and for a model with different source geometries this choice will always be problematic. For the purposes of this comparison, we used a structural index of zero (which should be appropriate for the vertical susceptibility contrasts). Using a larger structural index yielded estimates of source location that were deeper, but with a similar amount of scattering in the solutions. Solutions from the 3D Euler deconvolution were accepted if the x, y locations were within 2.5 km of peaks in the grid of k_h, if the estimated depths were between 0 km and 15 km, and if the standard deviation of the estimated depth was less than 10% of the estimated depth. For both the proposed and classic 3D Euler deconvolution methods, the plotted profiles show all calculated solutions in gray, with the accepted solutions (based on the strategies described above) plotted in black.

In profile A (Figure 5a), depth estimates from the derivatives of the tilt angle corresponding to magnetization contrasts in the basement at x = 70 km and x = 170 km form tight clusters slightly below the basement surface. The estimates of the structural index are around 0.5, higher than we might expect for these source geometries. Other clusters of depth estimates, corresponding to topographic features in the basement surface, are scattered on either side of the basement. The 3D Euler solutions for this profile show a similar amount of scatter, though a greater proportion of source location clusters show no corre-

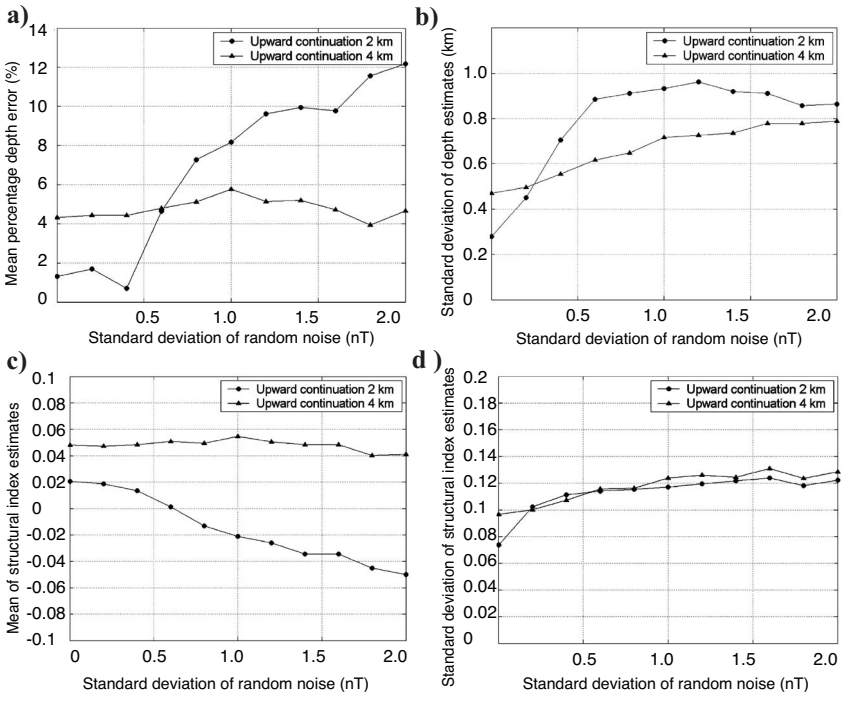

Figure 3. Accuracy of depth and structural index estimates for simple prism model data sets (Figure 2) corrupted with different levels of random noise, using different continuation distances; (a) Percentage error in depth estimates; (b) standard deviation of depth estimates; (c) error in structural index estimates; (d) standard deviation of structural index estimates.

spondence with the true basement depth. For cross-section B (Figure 5b), the depth estimates from the derivatives of the tilt angle method at x less than 100 km (where the basement surface is relatively shallow) exhibit several kilometers of vertical scatter. The 3D Euler deconvolution solutions for this area are less scattered and generally lie within about 1 km of the model basement depth. For x greater than 100 km, the source locations from both methods form tighter clusters located near the model basement.

Field example

We have applied the tilt angle derivatives method to aeromagnetic data from north-central Namibia, the same data used by Verduzco et al. (2004) in their work on the tilt angle. The 12 × 14 km study area contains the Erindi gold prospect, located on the eastern boundary of the Central Zone of the Damara Orogen. Gold occurrences in this area are associated with metamorphism and magmatic intrusions within the Swakop Group marbles. The associated ore minerals are dominated by pyrrhotite, pyrite, and magnetite, thus the mineralized zones are highly magnetic. Basement is covered by extensive soil and calcrete, up to 10 m thick. The total magnetic intensity (TMI) anomaly map is a 50-m grid derived from a survey with a flight-line spacing of 200 m, flying height of 80 m, and flight-line direction north-south. The data were reduced to the pole (Figure 6a) using a magnetic inclination of −62° and declination −12° (Verduzco et al., 2004).

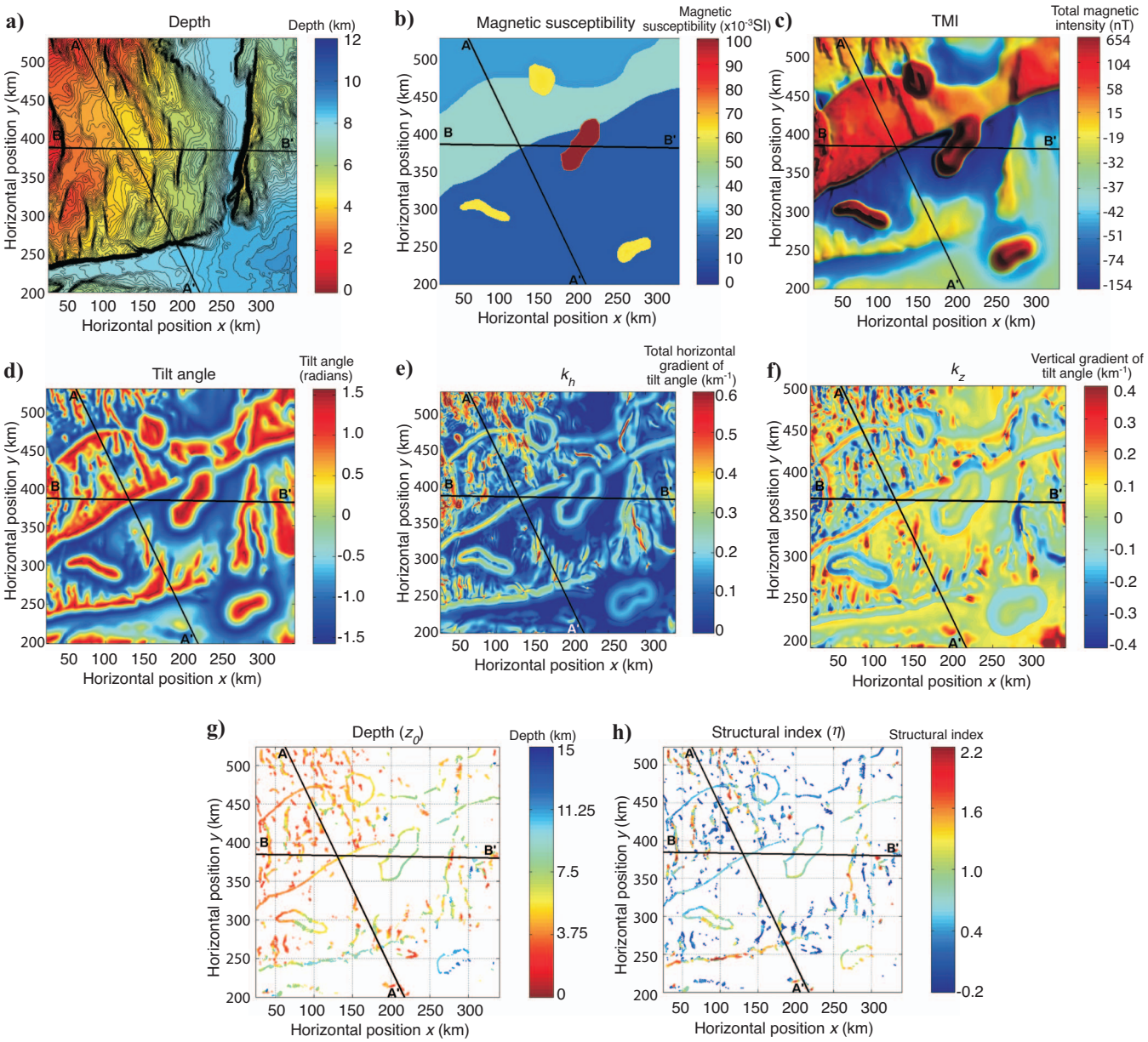

Figure 4. (a) Topographic data of the Bishop model; (b) magnetic susceptibility of model basement; (c) total magnetic anomaly data of the Bishop model; (d) tilt angle derivative; (e) total horizontal derivative of the tilt angle; and (f) vertical derivative of the tilt angle. (g) Map view of the estimated source location; and (h) estimated structural index. Line segments AA′ and BB′ establish the location of the magnetic profiles shown, respectively, in Figure 5a and b.

Figure 6b shows the tilt angle, with the total horizontal and vertical gradients of the tilt angle in Figure 6c and d. The grid of k_h (Figure 6c) is equivalent to the grids shown in Figures 4 and 5 of Verduzco et al. (2004). The estimates of source location and structural index derived from the derivatives of the tilt angle method are shown in Figure 6e and f. These estimates are derived from 13×13 point windows (600×600 m), from window locations where the window center lies within 200 m of peaks in the grid k_h. As before, we adopted the following criteria to identify and accept solutions. We accepted solutions if the horizontal coordinate estimates were within 200 m of peaks in the grid of k_h, if the estimated depths were between 0 and 300 m, if the estimated structural index was between -0.2 and 2.2, and if the estimated standard deviation, as a percentage of the estimated depth, was less than 25%.

Estimates of the structural index vary between different features (Figure 6f), with values typically in the range 0–1.5. The estimated depth to magnetic sources (Figure 6e) is consistently in the range from 0 to 200 m beneath the surface, consistent with the interpretation of Verduzco (2003) and Verduzco et al. (2004). These authors present the results of profile modeling through three linear features in the study area, interpreted as steeply dipping mineralization veins within the Swakop marble and metasediments. The veins can be modeled with dike-like geometries, with depths-to-top varying along strike from near outcrop up to 150 m depth (Verduzco et al., 2004). Figure 7 shows profile NN′, defined in the same location as profile P2 of Verduzco et al. (2004). The plotted source locations have been extracted from a band 200 m on either side of the profile location, and projected onto the profile perpendicular to the profile direction. Verduzco et al. (2004) presented two alternative models for this profile, modeling the sources of the main anomalies both as thin dike-like bodies or broader blocks. The profile for solutions using a window size of 13×13 points shows a cluster of source locations corresponding to the highest amplitude TMI anomaly on the profile, and also corresponding to a thin dike at a depth of about 50 m in the forward model. The estimated structural indices for these source locations are generally in the range from 0.5 to 1, suggesting a source geometry similar to a thin dike. The modeled profiles presented by Verduzco et al. (2004) show several other structures, for which our method produces solutions that appear scattered in cross-section view but form part of a coherent linear trend in map view. These

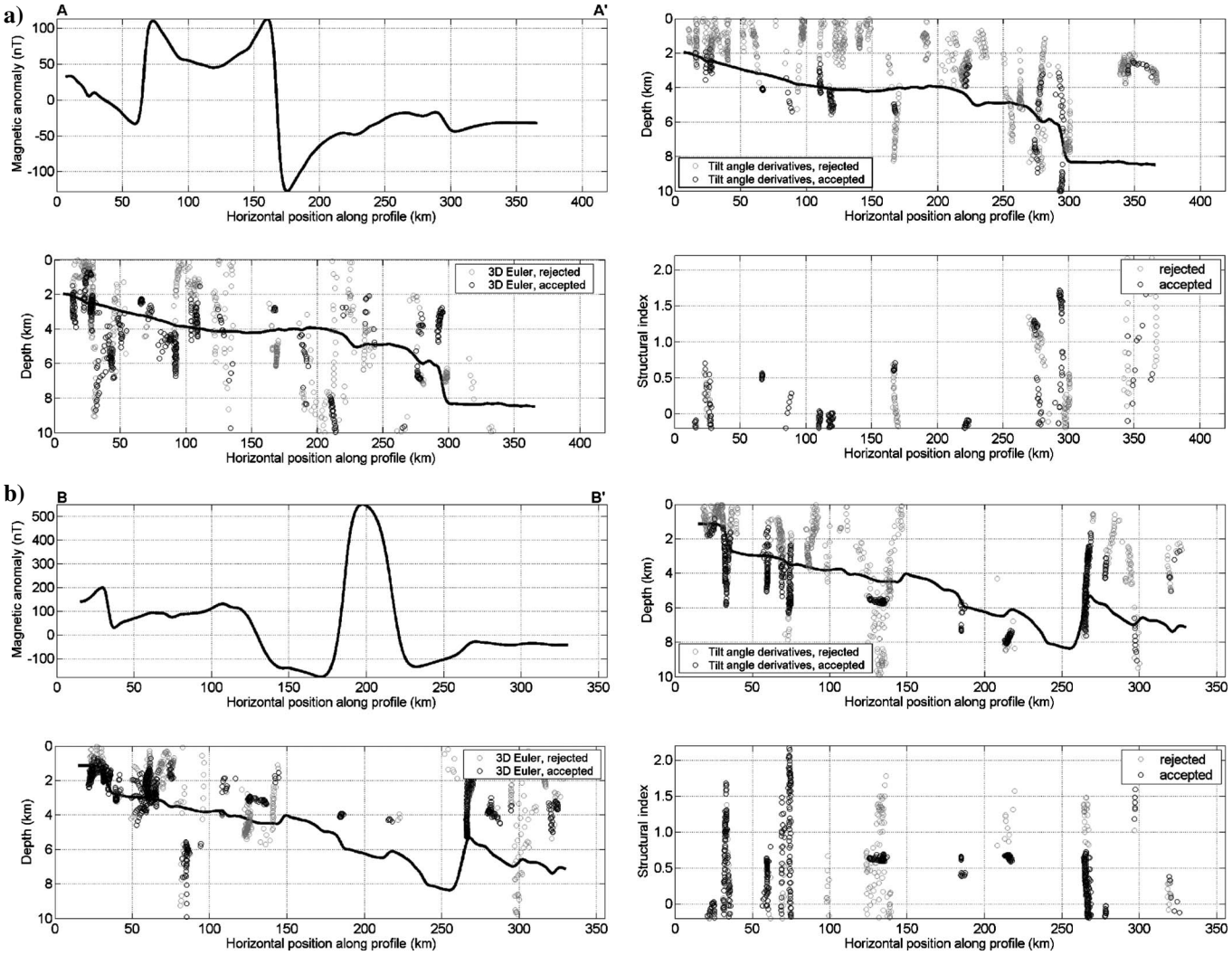

Figure 5. The first panel in each group shows magnetic data for cross section (a) AA′ and (b) BB′, shown in Figure 4. The second and third panels display the estimated source locations derived from tilt angle derivatives and 3D Euler deconvolution respectively. The true basement is shown in black line. The fourth panel shows the estimated structural indices.

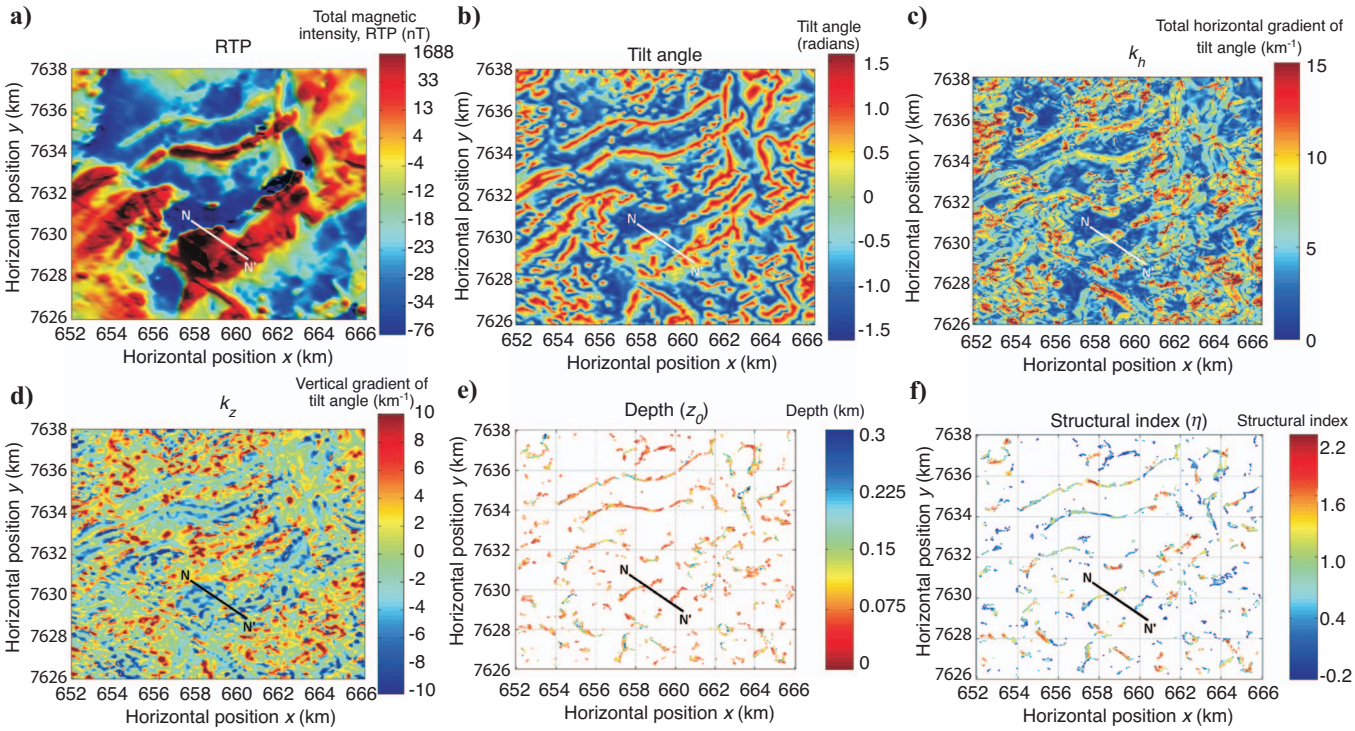

Figure 6. (a) Reduced to the Pole magnetic anomaly data from north-central Namibia; (b) tilt angle derivative; (c) total horizontal derivative of the tilt angle; (d) and vertical derivative of the tilt angle. (e) Map view of the estimated source location (f); and structural index.

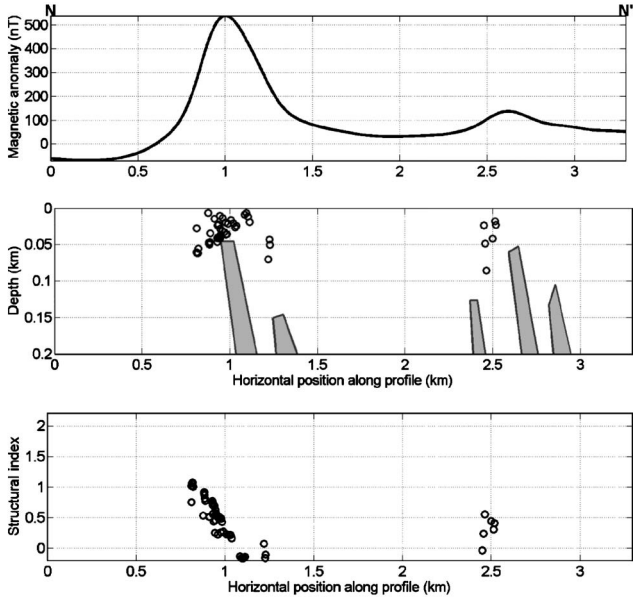

Figure 7. The upper panel shows magnetic data for cross-section NN′ shown in Figure 6. The lower panels display the estimated source locations and structural indices, superimposed on the forward-modeled interpretation (shaded polygons) of Verduzco et al. (2004).

more subtle structures appear to be at the limit of resolution for our method, even when a smaller window size is used. However, the comparison between our results and the modeled profiles does suggest that our method can be used to extrapolate the results of 2D profile modeling in three dimensions with some confidence.

CONCLUSION

We present a new technique for the interpretation of gridded magnetic data based on derivatives of the tilt angle. The method yields a linear equation to estimate the horizontal location and depth of magnetic sources without a priori information about the nature of the sources (structural index). Information about the nature of the sources is subsequently obtained by finding structural indices using the estimated source location parameters. The method was tested using synthetic anomaly data with and without random noise over different magnetic models. The method was also tested using the theoretical data of the Bishop model. In all cases, the method estimated the source parameters with adequate precision. Because the method utilizes second order derivatives of the magnetic anomaly, it is sensitive to noise in the data. To produce more reliable results, we apply an upward continuation of the magnetic anomaly field when significant noise is present. As with many similar methods, our method is

theoretically independent of magnetization direction and is suitable for the interpretation of single sources or multiple magnetic sources that do not give rise to interfering anomalies. We demonstrated the practical utility of the method by applying it to magnetic data from Namibia. The results of our method show broad correlation with previous published results using interactive forward modeling.

ACKNOWLEDGMENTS

We greatly appreciate constructive and thoughtful comments of the associate editor Valéria Barbosa, reviewer Afif Saad, and three other anonymous reviewers.

REFERENCES

Blakely, R. J., 1995, Potential theory in gravity and magnetic applications: Cambridge University Press.

Blakely, R. J., and R. W. Simpson, 1986, Approximating edges of source bodies from magnetic or gravity anomalies: Geophysics, **51**, 1494–1498.

Cooper, G. R. J., and D. R. Cowan, 2006, Enhancing potential field data using filters based on the local phase: Computers and Geosciences, **32**, 1585–1591.

Fedi, M., 2007, DEXP: A fast method to determine the depth and the structural index of potential fields sources: Geophysics, **72**, no. 1, I1–I11.

Fairhead, J. D., S. E. Williams, and G. Flanagan, 2004, Testing magnetic local wavenumber depth estimation methods using a complex 3D test model: 74th Annual International Meeting, SEG, Expanded Abstracts, 742–745.

FitzGerald, D., A. Reid, and P. Mclnerney, 2004, New discrimination techniques for Euler deconvolution: Computer and Geoscience, **30**, 461–469.

Miller, H. G., and V. Singh, 1994, Potential field tilt — A new concept for location of potential field sources: Journal of Applied Geophysics, **32**, 213–217.

Nabighian, M. N., V. J. S. Grauch, R. O. Hansen, T. R. LaFehr, Y. Li, J. W. Peirce, J. D. Phillips, and M. E. Ruder, 2005, The historical development of the magnetic method in exploration: Geophysics, **70**, no. 6, 33ND–61ND.

Nabighian, M. N., and R. O. Hansen, 2001, Unification of Euler and Werner deconvolution in three dimensions via the generalized Hilbert transform: Geophysics, **66**, 1805–1810.

Ravat, D., 1996, Analysis of the Euler method and its applicability in environmental magnetic investigations: Journal of Environmental Engineering Geophysics, **1**, 229–238.

Reid, A. B., J. M. Allsop, H. Granser, A. J. Millet, and I. W. Somerton, 1990, Magnetic interpretation in three dimensions using Euler deconvolution: Geophysics, **55**, 80–91.

Reid, A. B., D. Fitzgerald, and G. Flanagan, 2005, Hybrid Euler magnetic basement depth estimation: Bishop 3D tests: 75th Annual International Meeting, SEG, Expanded Abstracts, 671–673.

Salem, A., and D. Ravat, 2003, A combined analytic signal and Euler method (AN-EUL) for automatic interpretation of magnetic data: Geophysics, **68**, 1952–1961.

Salem, A., D. Ravat, R. Smith, and K. Ushijima, 2005, Interpretation of magnetic data using an enhanced local wavenumber (ELW) method: Geophysics, **70**, no. 2, L7–L12.

Smith, R. S., and A. Salem, 2005, Imaging the depth, structure, and susceptibility from magnetic data: The advanced source parameter imaging method: Geophysics, **70**, no. 4, L31–38.

Smith, R. S., A. Salem, and J. Lemieux, 2005, An enhanced method for source parameter imaging of magnetic data collected for mineral exploration: Geophysical Prospecting, **53**, 655–665.

Smith, R. S., J. B. Thurston, T. F. Dai, and I. N. MacLeod, 1998, iSPI™ — the improved source parameter imaging method: Geophysical Prospecting, **46**, 141–151.

Stavrev, P., and A. Reid, 2007, Degrees of homogeneity of potential fields and structural indices of Euler deconvolution: Geophysics, **72**, no. 1, L1–L12.

Thompson, D. T., 1982, EULDPH: A new technique for making computer-assisted depth estimates from magnetic data: Geophysics, **47**, 31–37.

Thurston, J. B., and R. S. Smith, 1997, Automatic conversion of magnetic data to depth, dip, susceptibility contrast using the SPI™ method: Geophysics, **62**, 807–813.

Thurston, J. B., R. S. Smith, and J. C. Guillon, 2002, A multimodel method for depth estimation from magnetic data: Geophysics, **67**, 555–561.

Verduzco, B., 2003, The interpretation of aeromagnetic data over the Erindi area, Namibia: MSc. thesis, University of Leeds.

Verduzco, B., J. D. Fairhead, C. M. Green, and C. MacKenzie, 2004, New insights into magnetic derivatives for structural mapping: The Leading Edge, **23**, 116–119.

Williams, S. E., J. D. Fairhead, and G. Flanagan, 2002, Realistic models of basement topography for depth to magnetic basement testing: 72th Annual International Meeting, SEG, Expanded Abstracts, 814–817.

———, 2005, Comparison of grid Euler deconvolution with and without 2D constraints using a realistic 3D magnetic basement model: Geophysics, **70**, L13–L21.